Article

Not peer-reviewed version

Optimizing Tensile Properties and Hardness of Inconel 718 by Cold Rolling

Wakshum Mekonnen Tucho * , Anders Thon Sletsjøe , Navid Sayyar , Vidar Hansen

Posted Date: 7 March 2024

doi: 10.20944/preprints202403.0419.v1

Keywords: tensile properties; microstructure; hardness; texture; microscopy; characterization

Article

Optimizing Tensile Properties and Hardness of Inconel 718 by Cold Rolling

Wakshum Mekonnen Tucho *, Anders Thon Sletsjøe, Navid Sayyar and Vidar Hansen

Department of Mechanical and Structural Engineering and Materials Science, Faculty of Science and Technology, University of Stavanger, 4036 Stavanger, Norway
* Correspondence: wakshum.m.tucho@uis.no

Abstract: The as-received commercial Inconel 718 material was solid solution heat treated (ST), cold rolled (CR), and precipitation hardened (PH) to investigate the effects of deformation on tensile properties, hardness, and texture. Three sets of specimens (0%, 20% and 50% CR) were STed at 1100 °C/1h, CR and aged (720 °C/8 h + 650 °C/8 h) for the analysis. Ultimate tensile strength (UTS), 0.2% yield strength (YS) and elongation of 50% deformed condition were 1645 MPa, 1512 MPa, and 3.8 %, respectively. The 20 % deformation resulted in a balanced UTS (1348 MPa), YS (1202 MPa) and elongation (11%). Contributions of precipitation hardening to the strength was decreasing, while contribution of CR increases with increasing percentage of deformation. Correspondingly, the size and quantities of γ'' decreased with increasing deformation level. In CR specimens, a high density of nano/micro twins were generated with the twin planes oriented perpendicular to the RD-ND surface. The preferred rotation of the crystals generated the gradient of orientation and internal features of the large austenitic grains. The cross-slip of screw dislocations induced a complete β-fibre, consisting of {110}<112>, {112}<111>, and{123}<634>, with doubled intensity at higher deformation. In addition, the specimens tended to be highly susceptible to the twinning-induced orientation emerged by a predominant <110>∥ND. An incomplete but intense α-fibre clustered between {110}<001> and {110}<112> was characterized in the as-deformed condition. Besides achieving highest strength, the current work demonstrates the effects of CR on the material strength without the complex influences of δ precipitate.

Keywords: tensile properties; microstructure; hardness; texture; microscopy; characterization

1. Introduction

Inconel 718 is a precipitation strengthened nickel-base superalloy with high strength, excellent creep, and corrosion resistance [1,2]. The alloy is an ideal choice in a wide range of service temperatures, especially in energy and in aviation sectors due to its stable mechanical properties as high as 650 °C [3,4]. The as-produced Inconel 718 generally consists of austenite (fcc) matrix and some primary segregated phases, mainly Laves, and carbides. Prior to application, the segregated phases, specially Laves need to be dissolved as they have determinantal effects on the mechanical properties. An optimum microstructure and mechanical strength of the alloy can be obtained by performing two steps of post-fabrication heat treatments, which are solid solution heat treatment (ST) and aging (also known as precipitation hardening) [5–8]. After the successive heat treatments, the main desired phases to precipitate in the austenite matrix of the alloy are fcc $L1_2$ ordered $Ni_3(Al,Ti)$ γ' and the bct D022 ordered Ni_3Nb γ''. The latter (γ'') is regarded as the main strengthening phase with the ratio of 4:1 compared to the former (γ'). The other phase precipitated under certain temperature range in Inconel 718 is the δ phase, which is stable unlike the metastable γ'' phase. The δ phase has an orthorhombic (D0a) crystal structure with a similar stoichiometry of Ni_3Nb as that of γ'' and it is often regarded as another strengthening phase in Inconel 718 [4,9].

Further strengthening of Inconel 718 can be achieved by combining heat treatment with work hardening, through cold rolling. The cold rolling primarily induces dislocation networks and vacancies in the material, which are known to enhance the material properties such as tensile strength, creep resistance and hardness at the expense of ductility. These properties, however, are affected by the distribution and morphology of the hardening phases, which are γ′, γ″ and δ. It is thus, important to understand how cold rolling affects precipitation of these phases. Cold rolling results in plastic deformation, leading to changes in the morphology of grains and the grain boundary regions. The mechanism of deformation is responsible for the generation of dislocations, elongation of grains and the changes that occurred in the internal structure within the grains. In addition, most of the grains tended to be reoriented with respect to the directions of the applied stresses during rolling. These changes normally expected to affect the nucleation, distribution and morphology of the precipitation hardening in Inconel 718.

Most researchers [10–12] studied the effects of δ phase precipitation in a cold rolled Inconel 718 on microstructure and mechanical strength. According to these reports, the nucleation sites and precipitation of δ phase can be enhanced, followed by depletion of Nb that greatly reduces the number and size of γ″ precipitates because of global recrystallization and transformation of γ″ to δ phase. The increment in nucleation sites for δ phase is believed to be due to the growth in the fraction of grain boundaries [12]. Moreover, cold rolling process significantly reduces the content of γ″ with increasing percentage of thickness reduction in the temperature range of solution and ageing treatments that promotes precipitation of δ phase. The effects of δ phase on the material properties are however controversial since some reports show affirmative [12] while others considered detrimental [11]. On the positive side, δ phase can improve mechanical properties since it pins grain boundaries and limit grain size by contributing to the grain homogenization [12]. On the contrary, δ phase is brittle and can adversely affect the plasticity of IN718 as well as its strength [11,13,14]. Besides, the presence of δ phase complicates understanding of the effects of the main hardening phases under the deformation process. In view of these, it worths investigating the effects of cold rolling on the microstructure and mechanical properties in the absence of δ phase.

This work deals with the effects of cold rolling on the microstructural features, crystallographic orientation, and mechanical properties of Inconel 718. To understand the influence of deformation in an unambiguous approach, the temperature range for the heat treatment schemes were chosen in such a way to avoid the precipitation of δ phase. The investigations in this work were partly based on the master's thesis project of the second co-author [15].

2. Experimental Methods

2.1. The Material

The initial material was Inconel 718 components of 7/8″ bolts and nuts supplied by Scandinavian Fittings and Flanges (SFF), located in Sandnes, Norway. The composition of Inconel 718 alloy includes, 17.86 Cr, 5.02 Nb, 2.99 Mo, 0.96 Ti, 0.51 Al, 0.05 Cu, 0.07 Mn, 0.014 C, 0.06 Si, 0.008 P, 0.0025 B, 0.0005 S and with Ni compromises the balance in wt.%. The material was produced by VIM+VAR (vacuum induction melting + vacuum arc remelting) method. After production, the specimens were solution annealed at 1030°C for 1.5h (water quenched) and then precipitation hardened at 780°C for 6.3h (air cooled). Finally, the threads of the bolts and nuts were formed by cold rolling. Here after the corresponding specimens will be called original condition (OC). The microstructure of the initial material is shown in Figure 1. The OC specimen consists of equiaxed grains, numerous annealing twins, and some segregated phases along the grain boundaries and within the grains (Figure 1a). EDS analysis shows that the particles are rich in Nb and Ti, indicating a carbide type phase. Furthermore, TEM image (Figure 1b) reveals hardening precipitates, mainly γ″ phase with an average length of 51 nm.

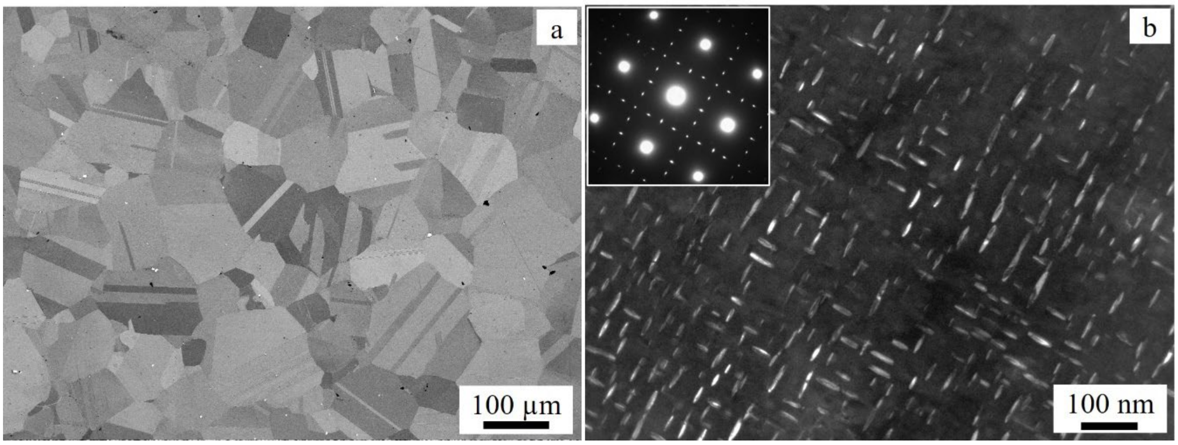

Figure 1. Microstructure of the initial material (a) SEM image and (b) TEM dark field image, showing γ'' phase precipitates. The insert in (b) is a diffraction pattern in zone axis.

2.2. Heat Treatment and Cold Rolling

The specimens for the tests were obtained by machining the bolts (OC) to a rectangular shape with the dimension in the range of length (134-145 mm), width (9.5-14.3 mm) and thickness (4.7-5.7 mm). For the experimental investigations, the machined OC specimens were subjected to heat treatment to attain a homogeneous state. This was achieved by performing a solid solution heat treatment (ST) at 1100 °C for 1h followed by water quenching. The heat treatments were performed in a Nabertherm furnace equipped with a K-type thermocouple. For the ST operations, the specimens were introduced after stabilizing the furnace to the target temperatures to avoid undesirable phase transformations at lower temperatures. The hardening phases and other segregated phases were believed to be entirely or partially dissolved and the material nearly attain in a strain-free condition. In addition, there might be some grain coarsening and the material became softer than the starting material (OC). The specimen at this stage is referred as homogenised condition or D0. The ST (D0) specimens were then cold rolled, and precipitation hardened to analyse the effects of deformation on the mechanical properties.

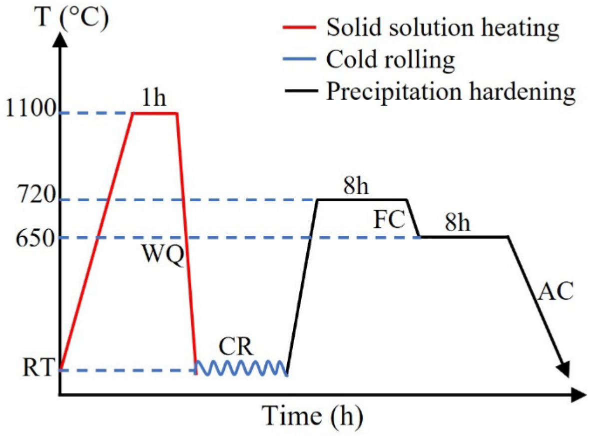

Figure 2. schematic profile of heat treatment regime and cold rolling – where T ≡ temperature, WQ ≡ water quenching, AC ≡ air cooling, FC ≡ furnace cooling and CR ≡ cold rolling.

The homogenised specimens (D0) were then divided into three sets depending on the level of deformation to be performed. These were undeformed (0%), 20% and 50% cold rolled. Each set was again divided into two – one set was subjected to two stages of aging and the other set was tested without aging. The aged specimens were suffixed by a letter 'A' to indicate aging. Cold rolling was

doi:10.20944/preprints202403.0419.v1

done by a Schmitz cold rolling mill. After several passes, the thickness was reduced to 4.15-4.62 mm and 2.59-2.81 mm for 20% and 50%, respectively.

Figure 3 shows the schematic of the specimens' coordinates, i.e., normal (loading), transverse, and rolling directions denoted as ND, RD, and TD, respectively. The rolling direction was parallel to the longer axis of the specimens. To provide a clear view of the microstructure in three dimensions, EBSD maps on each sample were performed from the rolling plane (RD-TD) and from the plane normal to the transverse direction (ND-RD). Large and small area acquisitions were carried out to study the grains' preferred orientation and grain boundaries. The diffraction data were subjected to grain dilation clean-up by TSL-OIM program to diminish the noise effect and acquire the orientation maps. EBSD data were further processed with the ATEX software (Analysis Tools for Electron and X-ray diffraction; Beausir and Fundenberger, 2017 [16]) to determine the texture evolution with respect to the deformation levels through the pole figures, and orientation distribution functions (ODFs). The harmonic series method was used for texture calculations. Presuming the orthonormal symmetry of rolled fcc material, the domain of Euler space was decreased to $0° < \varphi_1, \Phi, \varphi_2 < 90°$.

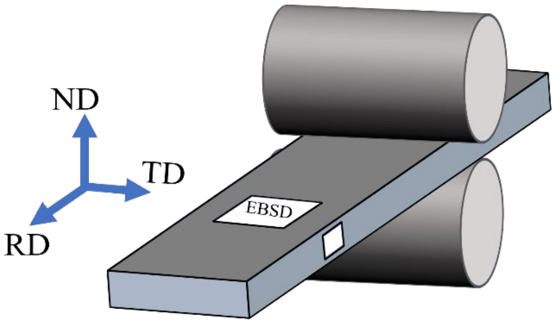

Figure 3. Schematic representation of rolling plate and the corresponding workshop axes.

The precipitation hardening treatment of each specimen was performed with two successive steps of heat treatments adopted for conventionally fabricated Inconel 718. The furnace was pre-heated to the aging temperature before introducing the ST specimens. The aging treatment was done, first at 720 °C for 8 h, and then the furnace was cooled down to 650 °C held the specimens for another 8 h. At the end of the soaking period, the specimens were removed from the furnace and cooled in the air. The specimens' descriptions are given in Table 1. Likewise, the schematics showing the heat treatment regimens and rolling is shown in Figure 2.

Table 1. Descriptions of specimens.

Sample ID	**ST**	**Def. (%)**	**PH**	
	1100°C /1h		**720°C /8h**	**650°C /8h**
D0	Yes	0	no	no
D0A	Yes	0	Yes	Yes
D20	Yes	20	no	no
D20A	Yes	20	Yes	Yes
D50	Yes	50	no	no
D50A	Yes	50	Yes	Yes
OC				

2.3. Characterization of Microstructure, Texture, and Phases

The microstructure, composition, and fracture surfaces of the specimens were analysed with Scanning Electron Microscopy (SEM), Gemini SUPRA 35VP (Carl Zeiss, Jena, Germany) equipped with EDAX Energy Dispersive X-ray Spectroscopy (EDS). The crystallographic orientation was studied using Electron Back Scattered Diffraction (EBSD) equipped on SEM using a TSL-OIM orientation imaging microscope system for analysis. Specimen preparation for the microstructure analysis consisted of mechanical grinding, fine polishing, and ultra-polishing with OP-S colloidal silica. EBSD mapping was performed at 20 kV, a working distance of 25 mm, a tilt angle of 70°, a scan step of 0.5-2 μm and a magnification of 100/200.

Phases and lattice defects were further investigated with Transmission Electron Microscopy (TEM), JEOL- 2100 (LaB_6 filament) (JEOL, Tokyo, Japan), operating at 200 kV. For TEM analysis, thin foils from the ND-TR surface were prepared, first by thinning down mechanically to a thickness of about 100 μm, and then 3-mm disks were punched from the thin foils. Finally, the disks were electropolished using a dual jet polishing system Struers TENUPOL-5 (Struers, Ballerup, Denmark) operated at 15 V and −30 °C in an electrolyte solution of 80% methanol and 10% perchloric acid.

2.4. Hardness Test

Vickers hardness tests were conducted on the RD-ND plane (parallel to the rolling direction) as shown in the illustration in Figure 3 under a load of 5 kg and a dwell time of 10 s. The hardness was measured with an Innovatest automatic hardness tester that allows many indentations to be done in a controlled and accurate manner. The interval between adjacent indentations were set at least to 3 times the average length of the diagonal following the standard specifications stated in ISO 6507-01 [17]. To avoid edge effects, the indentations were performed at more than 2.5 times the average length of the diagonal from the edges. For accuracy of the measurements, more than 70 imprints were conducted on each test specimens.

2.5. Tensile Test

The specimens for the tensile tests were obtained by machining the bolts (OC) to a rectangular shape with the dimension in the range of length (134-145 mm), width (9.5-14.3 mm) and thickness (4.7-5.7 mm). The uniaxial tensile tests were carried out parallel to the rolling direction at room temperature using Instron 5985 universal testing machine in accordance with test method A1 in ISO standard NS-EN ISO 6892-1:2019 [18] with a strain rate of 0.00025 s−1.

Elongation was measured using an external clip-on extensometer. Mazak CNC was used for machining the specimens. The geometry of the tested specimens is shown in Figure 4. Three tensile specimens were prepared for the 20% and 50% deformed cases. Due to shortage of material, only one specimen was available for the undeformed (D0A) case.

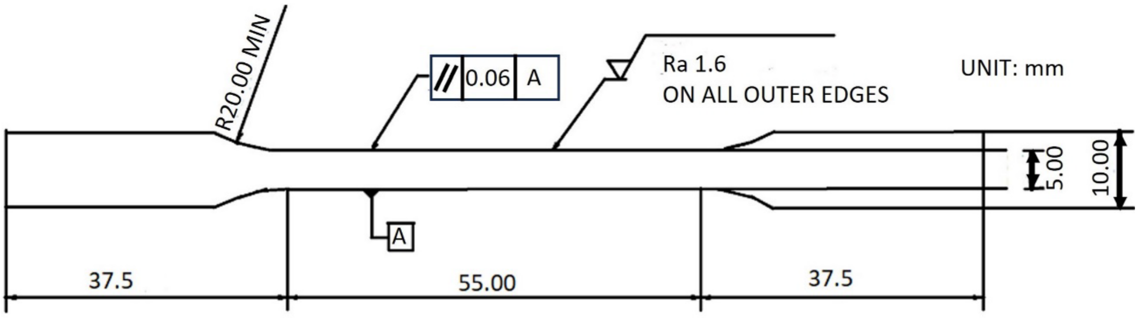

Figure 4. Schematic of tensile specimen.

3. Results

3.1. Microstructure

The microstructure of the specimens prepared from the RD-TD planes that were subjected to different conditions are shown by SEM images in Figure 5. For ease of visualizing, the images presented in the upper row are before aging while those images in the lower row are after aging. The images corresponding to 0%, 20% and 50% deformed specimens in the order from left to right for both rows. There are no noticeable differences in the grain structure between the specimens before and after aging for the same deformation. In general terms, the aging temperatures (720°C and 620°C) are not high enough for recrystallization that leads to changes in grain structures as shown in previous reports [19]. In the case of 0% deformation, D0 (Figure 5(a1)) and D0A (Figure 5(a2)), both specimens display similar main features, i.e., twins and grains. For the 20% (b1 & b2) and 50% (c1 & c2), the microstructures appear similar at the given magnification and resolution. The microstructures were stressed by the cold work process to the level that makes distinguishing the grain boundaries very difficult from the contrast. The equiaxed grains before the rolling were replaced by deformed grains. Most of the annealing twins formed by the ST were annihilated during the cold rolling process. But both sets of specimens (20% and 50% deformed) exhibit features that appear as strips across grains. Typical examples are shown in Figure 6.

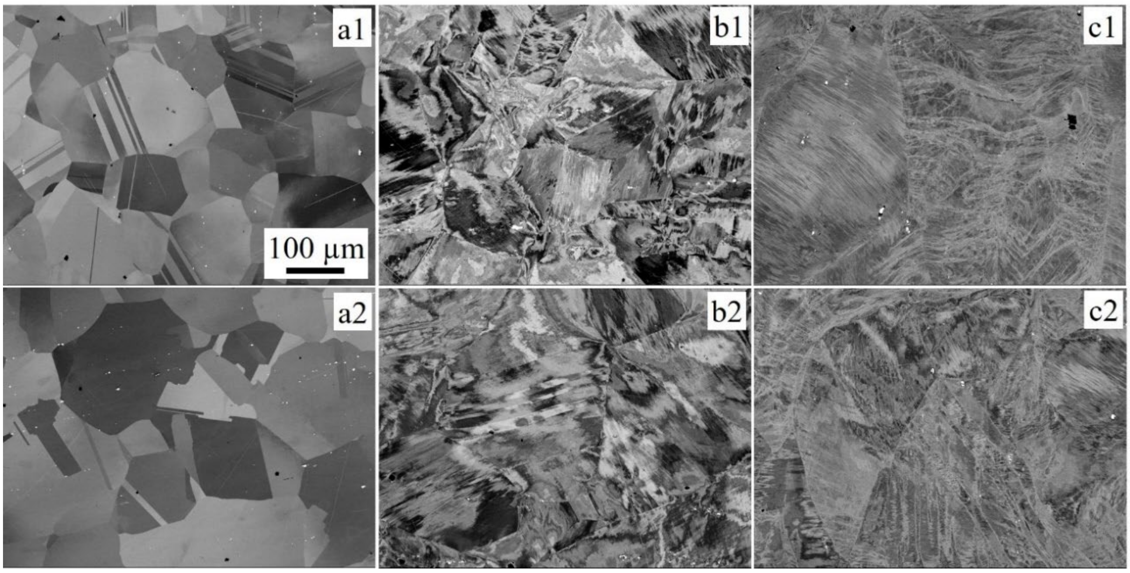

Figure 5. SEM-backscattered images. Undeformed (a1) before aging (D0), (a2) after aging (D0A), 20% deformed (b1) before aging (D20) (b2) after aging (D20A), and 50% deformed (c1) before aging (D50), and (c2) after aging (D50A). The images are all recorded at the same magnification (100x) and the scale bar shown in (a1) applies for the rest of the images too.

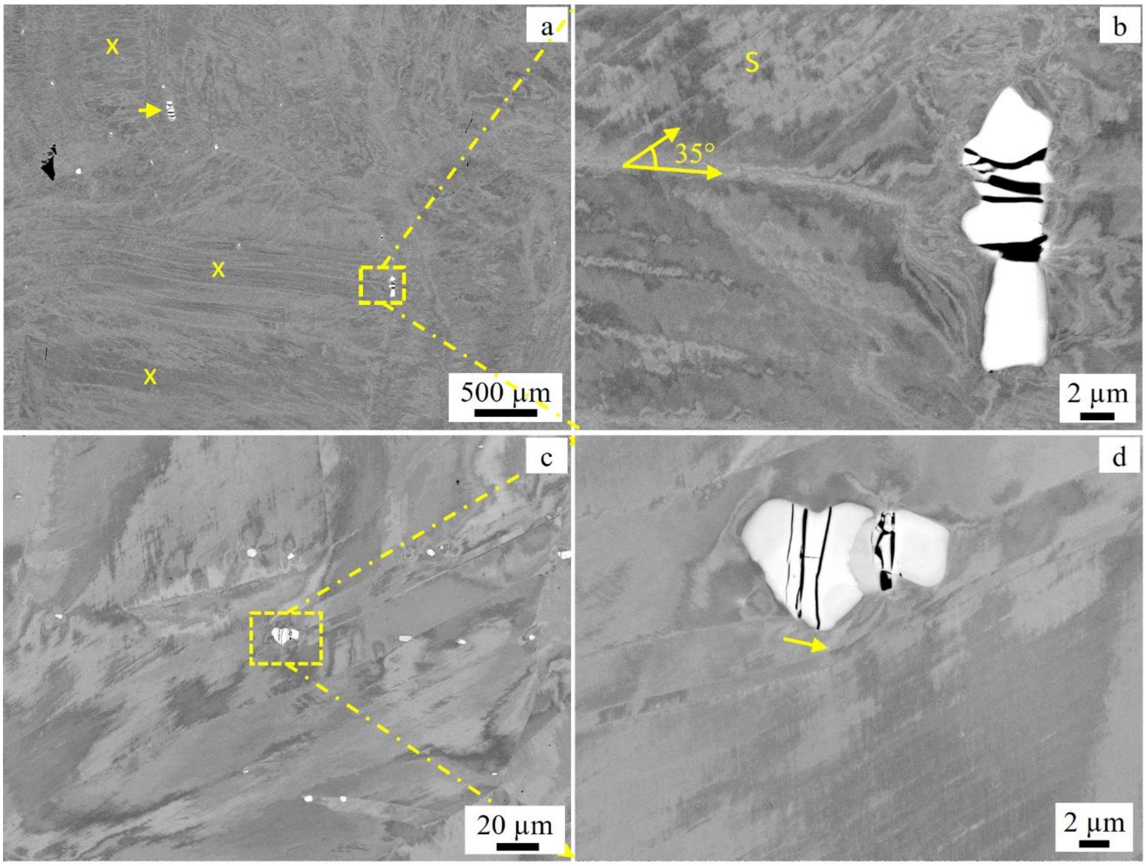

Figure 6. SEM-backscattered images of 50% deformed and aged (D50A) (a) low magnification and (b) high magnification. (c & d) are similar images of D20A. The 'X' marks in (a) indicate regions with elongated stripes appearing parallel to the direction of rolling while 'S' show some of the shear bands that are oriented by about 35° relative to the rolling direction. The approximate location of the image in (b) and (d) are shown by dashed boxes in (a) and (c).

Figure 6 shows typical microstructures of plastically deformed material in D50A and D20A. The regions marked by letter X in (a) consists of several strips of microstructures that are parallel to the rolling direction. These features appear to be either elongated grains or twins. The formation of the strips discontinued or blocked by the particle shown in white contrast. The particle is identified as carbide whose composition determined by EDS are 89 wt.% Nb and 7 wt.% Ti. The particle was cracked to accommodate the forces applied from the rollers as shown in the images. The cracks identified in most of such particles that are oriented normal to the rolling direction with their longer axis appearing parallel to the rolling direction. The particle indicated by an arrow in Figure 6a also experienced similar micro-fissuring. Because of the resistance from the particles, the region surrounding the carbide phase is heavily deformed as shown in Figure 6b. There are also other particles with the cracks oriented at an angle relative to the rolling direction as shown in Figure 6c,d. Figure 6d demonstrates how the rolling process dislocated the carbide particle and the strips bended around the bulged part of the particle. The cracks could be reoriented to the shown position may be after several passes of rolling. There are also numerous shear bands with a relative orientation of about 35° to the rolling direction (Figure 6b).

3.2. Hardening Precipitates

The phases precipitated after aging treatment are commonly observed with TEM. Bright Field (BF), and Dark Filed (DF) images of the specimens recorded with TEM are shown in Figure 7. The micrographs displaying the precipitates in the 0%, 20% and 50% deformed specimens are shown in Figure 7 (a, b), (c, d), and (e, f), respectively. It is well known that γ″ phase is the main hardening precipitates of Inconel 718 following aging treatment. The γ″ phase is generally nano-sized and ellipsoid in shape having major and minor axes. In the current work, the γ″ precipitates are short and resembles rods rather than ellipsoid in the Cred specimens. The other hardening phase precipitated after aging is γ′. It is round shape and finer than the γ″.

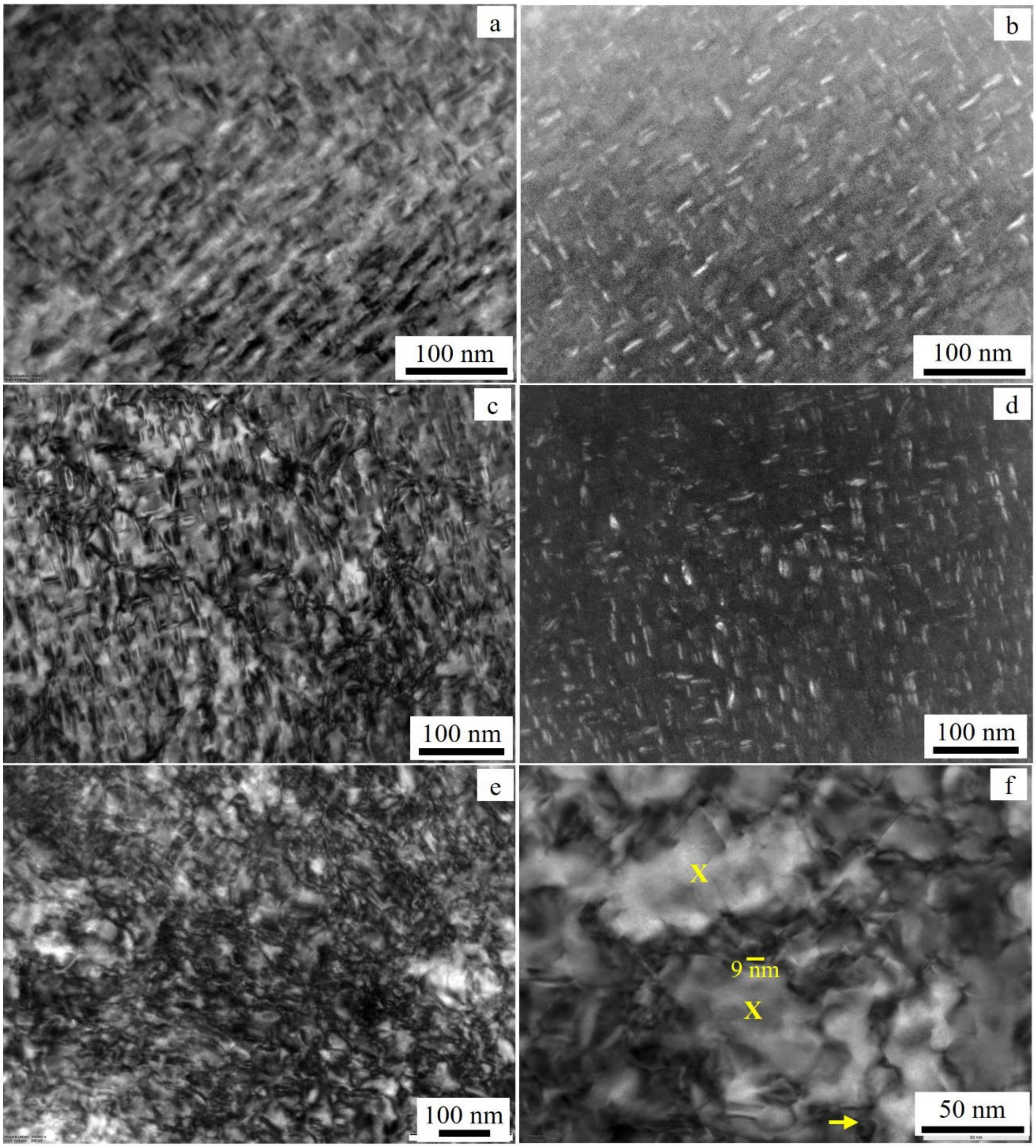

Figure 7. TEM image of γ″ recorded with the matrix oriented in [100] zone axis of D0A (a) BF, (b) DF; D20A (c) BF, (d) DF and D50A (e, f) BF. The 'X' marks in the magnified image of (f) show local strain-free areas. An example of a precipitate is shown by an arrow in (f).

As shown in Figure 7a,b the precipitates are uniformly distributed in the undeformed specimen. Likewise, the γ″ precipitates in the 20% rolled (c, d) are nearly distributed uniformly. However, the precipitates in the 50% rolled (D50A) appeared scattered as shown in (e, f) images. The microstructure of D50A contains localities with high level of strains and strain-free regions. Examples of strain and precipitate-free regions are marked by X in Figure 7f. The strained region consists of tiny precipitates of γ″ and dislocations that established high stress field regions. It can be inferred from the result that the sites for the nucleation of the hardening precipitates in D50A is the strained localities due to dislocations rather than the strain-free regions.

Quantity and size of the precipitates can affect the strengthening of the material as documented previously [20]. The size of γ'' precipitates in OC, D0A, D20A and D50A are 50.7±9.3, 9.5±2.1, 12.6±3.2, and 8.2±1.6 nm. respectively. The measurement showed that the precipitates formed in the reprocessed specimens (heat treated, rolled, aged) are smaller than the original material by about 5 folds. Comparison of the deformed specimens with the 0 deformed (D0A) shows slight differences. Specifically, the average size of γ'' phase in D20A is larger than those in D0A by about 3 nm (35%). The γ'' phase precipitated under D50A condition was however decreased by 1.3 nm (14%) and by 4.4 nm (54%) compared to D0A and D20A, respectively. It shows that the dimension of γ'' precipitate decreased with increasing percentage of deformation. This agrees well with similar observations in the literature [21].

The images shown in Figure 8 are typical diffraction patterns with the matrix oriented in [100] zone axis for (a) D0A, (b) D20A and (c) D50A, corresponding to 0%, 20% and 50 % deformed and aged specimens, respectively, presented in Figure 7. As documented in the literature [5,22], for an unambiguous identification of γ'' and γ', the matrix (γ phase) must be oriented in the <100> zone axis. The SADP shown in the insets of Figure 8a–c consists of strong reflections from the matrix (fcc - γ phase) oriented in [100] zone axis and the superimposed weaker superlattice reflections of the γ'' (bct) and γ' (primitive cubic) phases.

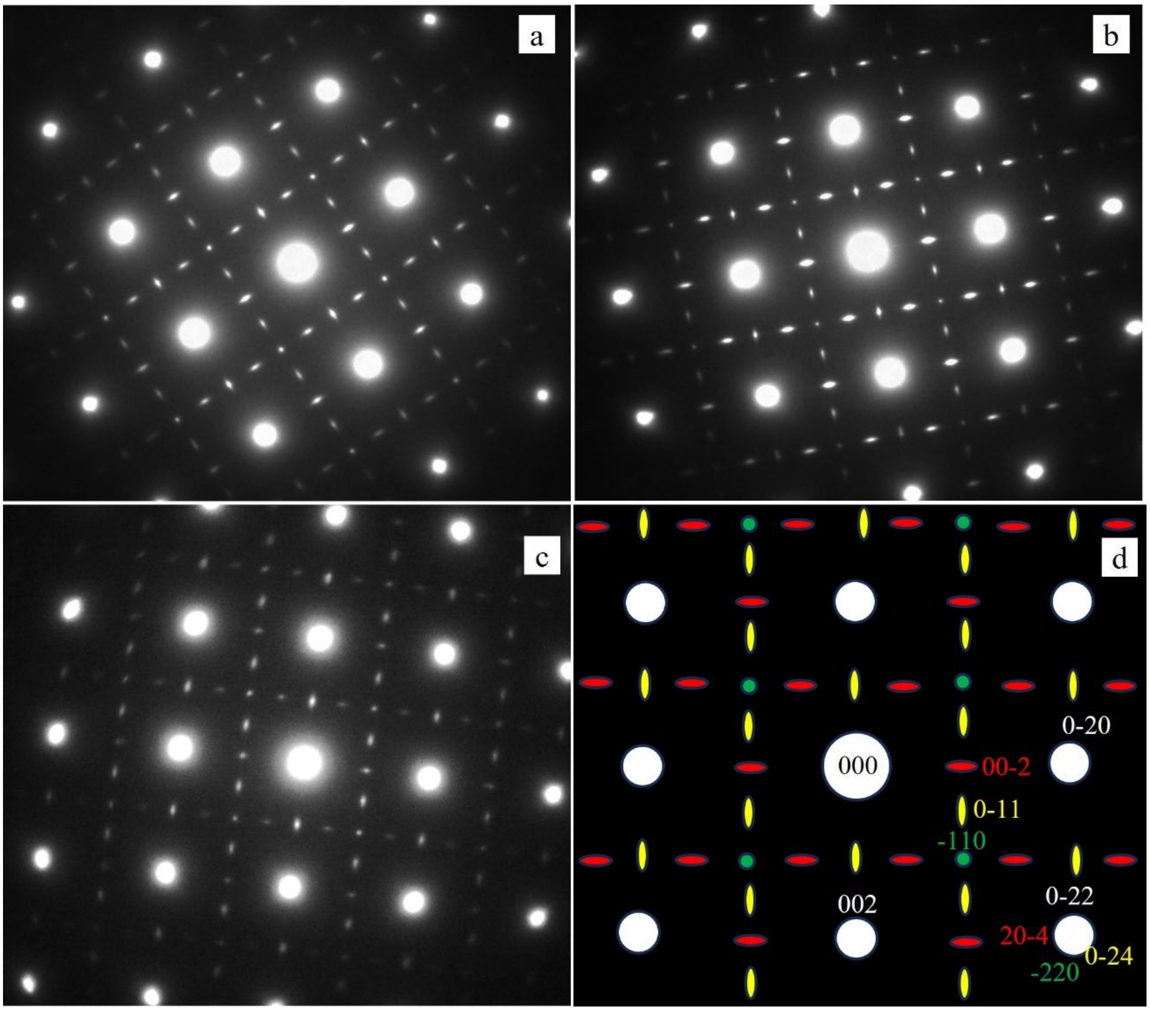

Figure 8. SADP of matrix in [100] for D0A (a), D20A (b) and D50A (c) corresponding to the images shown in Figure 7 (a, b), (c, d) and (e, f), respectively. (d) is the simulated SADP for the matrix [100]

showing the three variants of γ'' phase in [001] (green), [010] (yellow) and [100] (green). The white spots are reflections from the matrix.

Since the zone axes of γ'' are parallel with the matrix, rows of parallel spots of γ'' are superimposed with that of the matrix, there exits orientation relationship between the two phases: $(100)_{\gamma''}//(100)_{\gamma}$; $[010]_{\gamma''}//[010]_{\gamma}$. The simulated SADP of the three variants of the γ'' phase in [100] zone axis of the matrix is shown in Figure 8d. The white spots are corresponding to the matrix, whereas green, yellow, and red represent diffraction spots of γ'' phase variants in [001, [010] and [100] zone axis, respectively. Some of these diffraction spots are labelled with Miller indices to illustrate the overlapping of the spots (Figure 8d). The streaking of the lattice reflections of γ'' precipitates in [010] and [100] zone axis indicate that the precipitates are thin and ellipsoidal in shape. The spots in [001] direction however shows a disc since the zone axis is parallel to the c-axis of bct.

Qualitatively, the strength/size of the streaking of the γ'' precipitates of the three specimens are different as shown in Figure 8a–c. The spots of the reciprocal lattice reflections are larger in the order of D20A, D0A and D50A. Specifically, the reflection of γ'' phase corresponding to D50A are thin and short. These agree well with the quantitative analysis of the precipitates stated above. In the current study, identification of γ' was difficult, may be because of small size and fewer in quantity in the deformed specimens.

3.3. Hardness

The hardness measurement of all the samples tested is shown with the bar charts in Figure 9. For ease of visualizing the effects of aging, the bars in red and green colours present the hardness before and after the precipitation hardening heat treatments, respectively. As shown in the Figure, the hardness of the specimen with zero deformation, i.e., D0 increased from 165± 4.6 to 430±11.3 HV after aging treatment (D0A). This is about 265 HV or 160 % increment in hardness due to the formation of the hardening precipitates, mainly due to γ'' phase. The change in hardness after the two levels of deformation (D20 and D50) can be assessed by comparing with the hardness of the undeformed specimen (D0). The deformation magnitude of 20% (D20) resulted in hardness increment of 126 HV (76%) while the 50% of deformation enhanced the hardness by 252 HV (153%) compared to the zero deformed specimen (D0). The deformed specimens were further hardened after the aging treatment. The hardening precipitates strengthened D20A by 181 HV (62%) and D50A by 111 HV (27%) relative to the values before aging. Roughly speaking, the 20% (D20A) and 50% (D50A) rolled/deformed and aged specimens have shown an increment in hardness by about 42 HV (10%) and 98 HV (23%), respectively, compared to D0A (0% deformed & aged).

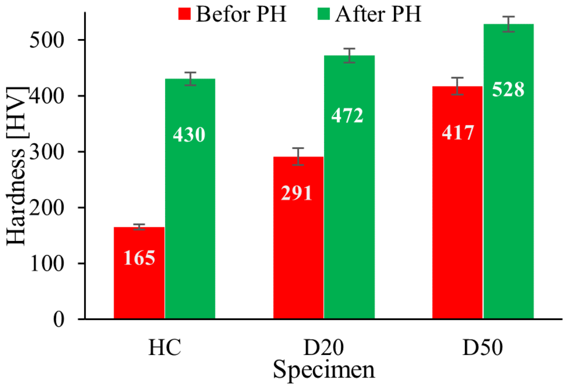

Figure 9. Hardness measurement – D0 is a 0% deformed, D20 and D50 are specimens deformed by cold rolling 20% and 50%, respectively. Red bars are before aging, whereas green bars are presenting hardness values after aging. PH stands for precipitation hardening.

3.4. Tensile Properties

A typical stress-elongation curves in Figure 10 show the tensile behaviour of the three sets of specimens (D0A, D20A and D50A) tested at room temperature. The inset is a bar chart for comparing the average values of the yield strength and UTS. The yield strength is represented by patterned bars while the UTS are shown with solid bars. Black, red, and green colours are used in the figure for marking the results related to D0A, D20A and D50A, respectively. The variations in the tensile properties have shown similar trends as that of hardness. The 0.2% YS of D20A was increased by about 242 MPa (25%) while the 0.2%YS of D50A increased by 552 MPa (or 58%) relative to D0A. Likewise, the UTS of D20A and D50A exceeded the UTS of D0A by 216 MPa (19%) and 513 MPa (45%), respectively. Deformation by 50% resulted in an increment of 310 MPa (28%) in YS and 297 MPa (22%) in UTS compared to the specimens deformed by 20% and aged (D20A). In agreement with hardness measurement, tensile strength is also increased proportionally with increasing percentage of deformation.

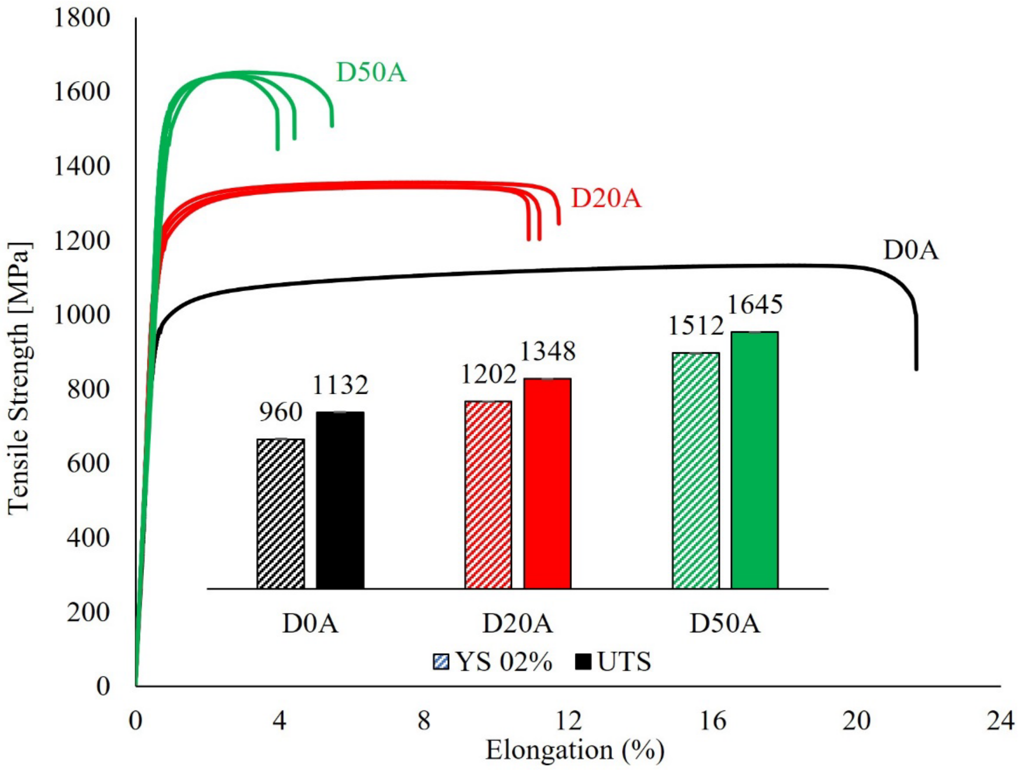

Figure 10. Tensile properties of the aged specimens are shown in line and bar charts. The labels at the top of the patterned bars and solid bars are the average values of yield strength and UTS, respectively.

The improvement in tensile strength after rolling and aging was achieved at the expense of ductility. As shown in Figure 10, the elongation is decreasing proportionally with increasing deformation level. The elongation of D50A is only 3.8 % compared to the elongation of D0A (21.1%), the reduction is about 17.3%. The 20% deformed (D20A) specimen has only decreased in elongation by about a half compared to the undeformed, D0A. Although deforming Inconel 718 by 50% enhanced the strength tremendously, the ductility was highly reduced. At the certain service condition, application of Inconel 718 may depend on a matter of choosing either strength or ductility. D20A however showed somewhat a balanced strength and ductility.

3.5. Deformation Texture Analysis

Figures 11a,d, 12a,d, and 13a,d show RD-TD orientation maps of all specimens. For better visualizing of the orientation, each micrograph includes small RD-projected IPF on its top right corner. Coarse equiaxed γ structure and a significant number of annealing twins randomly distributed are observed in D0 (undeformed, solution heat treated) in Figure 11a. The grain structure of the undeformed, but aged specimen (D0A) is shown in Figure 11d. Since the number of grains sampled is an important quantity for reliable texture measurements, the maximum intensity of the poles in Figures 11b,e cannot be expanded to the whole materials. The large grain size may be somehow problematic in obtaining reproducible results during the statistical measurements used by EBSD technique. However, when the stress is applied as shown for D20 for example, a preferrable rotation of individual fcc grains started to occur to align their <110>, i.e., the slip direction, with respect to ND (the loading direction). Significant orientations near <111> and <001>//RD are observed too, in small RD-projected IPFs of Figure 12a. The former implies the slip mode of deformation in fcc alloy which is predominantly happening in the most densely packed planes, i.e., {111}. As shown in Figure 13a for D50 (50% deformed), the mentioned rotation appears to be intensified with increasing deformation. Accordingly, stronger texture is expected in D50 compared to D20, as observed by the corresponding pole figures (Figures 12b and 13b). (111) pole maximum intensity increased from 2.25 to 2.96 times random, as the deformation increases from 20% to 50%.

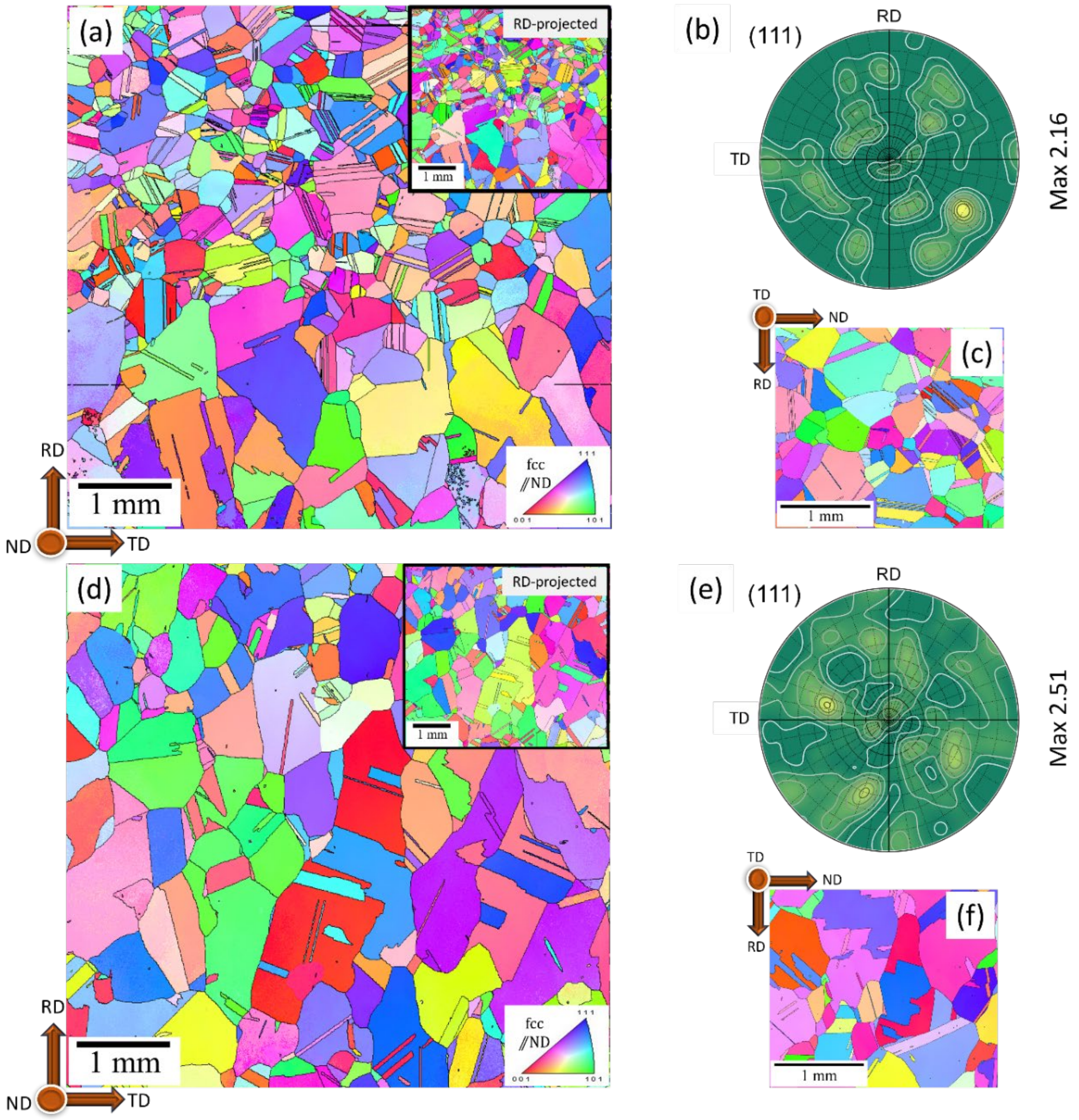

Figure 11. (a, d) RD-TD IPFs, (b, e)111 pole figures, and (c, f) ND-RD IPFs, corresponding to D0 and D0A, respectively.

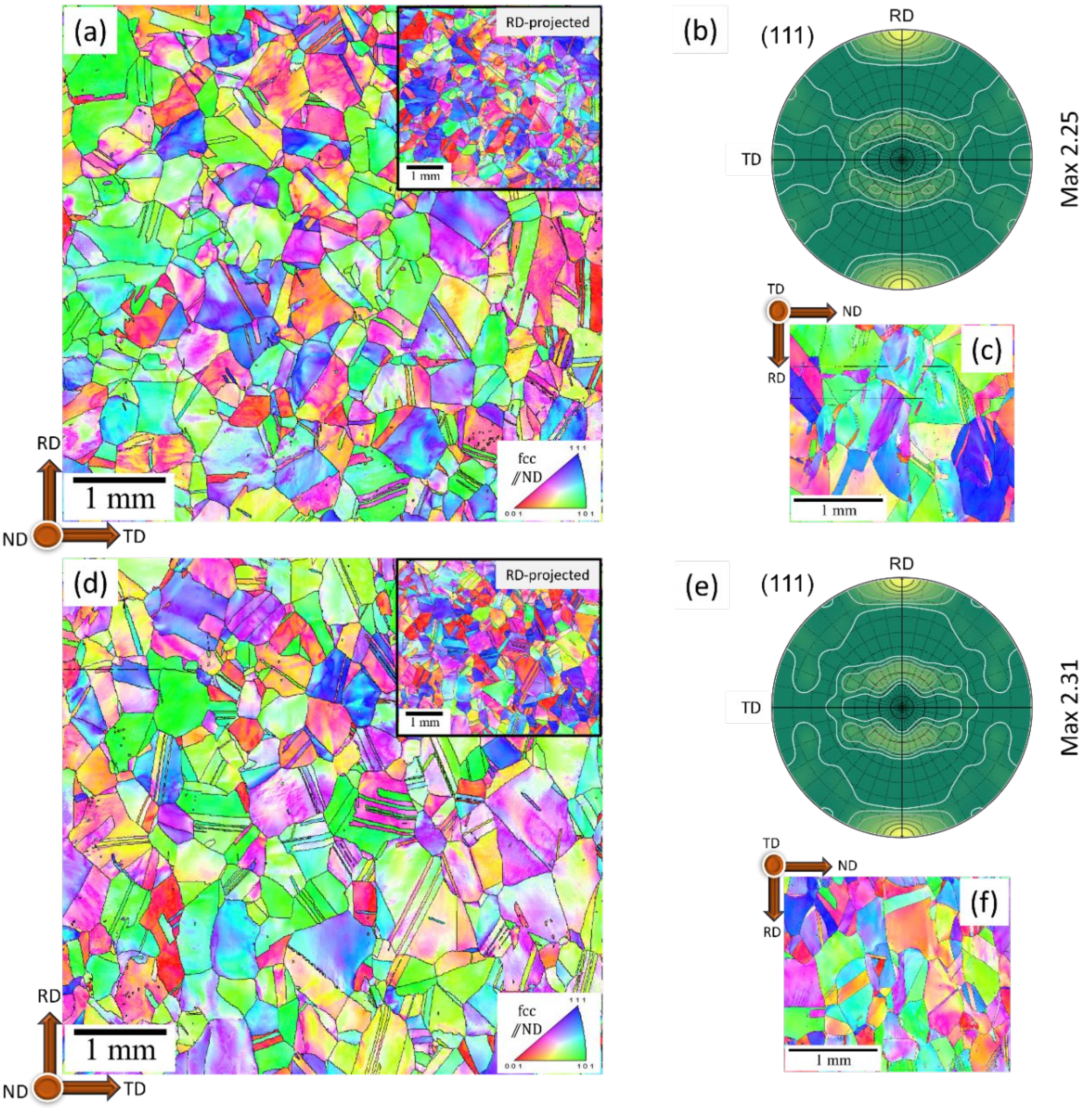

Figure 12. (a, d) RD-TD IPFs, (b, e)111 pole figures, and (c, f) ND-RD IPFs, corresponding to the specimens D20 and D20A, respectively.

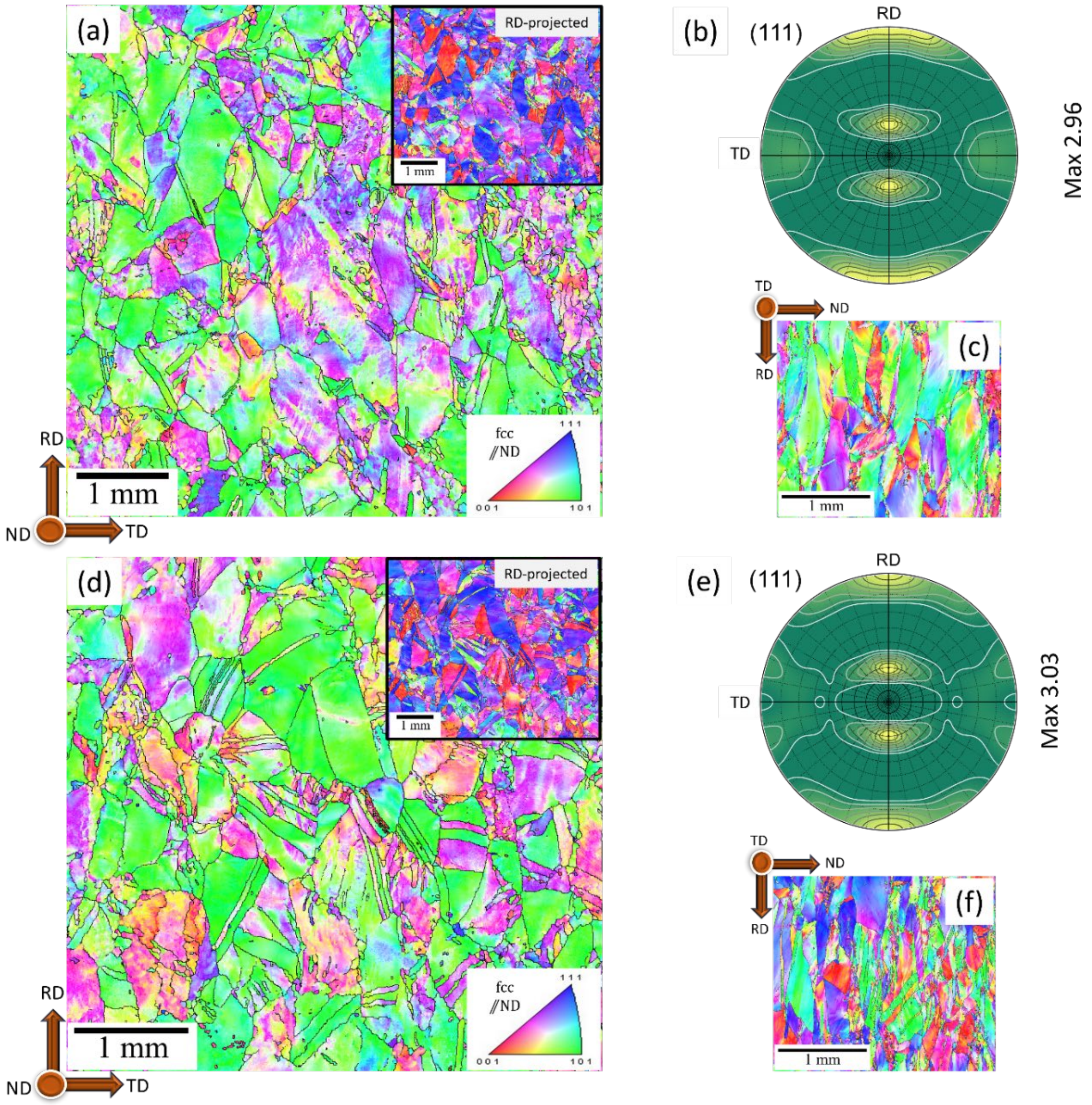

Figure 13. (a, d) RD-TD IPFs, (b, e) 111 pole figures, and (c, f) ND-RD IPFs, corresponding to the specimens D50 and D50A, respectively.

In addition, internal structure within the grains seems to be augmented by continuous generation of dislocations under the deformation mechanism, as shown in Figures 12a,d and 13a,d. This can also be noticed by comparing the individual coarse and equiaxed grains (Figure 11(c, f)) to the deformed crystals that are elongated towards RD (Figures 12c,f and 13c,f) in ND-RD IPFs. Aside from this morphological change, the gradient of crystals' orientation after rolling may suggest that each grain underwent non-uniform magnitude of rotation as the crystals' degree of freedom in different points can be limited mechanically by their boundaries. A messy and inhomogeneous structure known as deformation bands, seen in Figure 13a,c, could be generated when slip is running on several crystals at the same time. The rolling reduction up to 50% enhanced the density of deformation bands. The annealing twins appeared bent or even vanished as the degree of plastic deformation increased.

From the IPFs and pole figures in aged condition of D20A and D50A shown in Figures 12d–f and 13d–f, it can be inferred that their major initial preferred orientations were preserved. As the pole figures may not be able to differentiate the texture components properly, further analyses are required to identify the detailed texture evolution before and after heat treatment.

Evolution of Texture

For clarity, the ideal positions of basic texture components developed for cold-rolled fcc materials are schematically represented in the ODF sections of ϕ_2 =0°, 45°, and 63° in Figure 14.

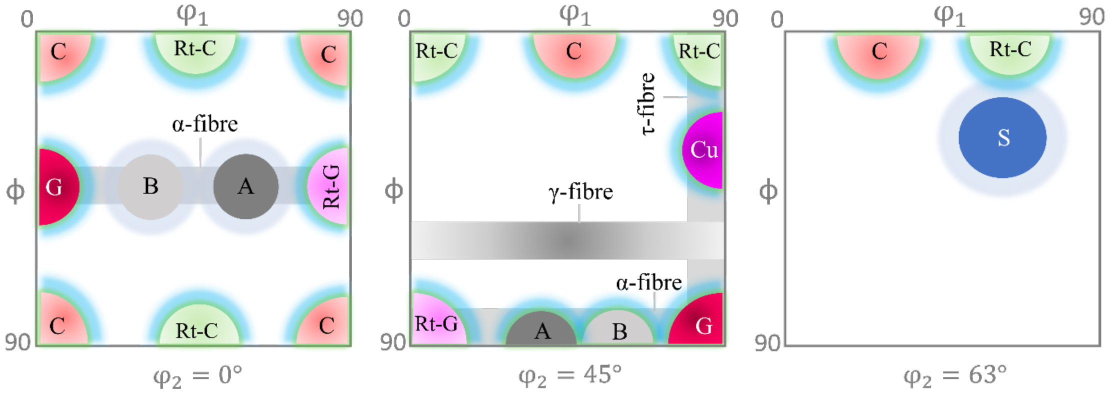

Figure 14. Schematic display of the typical texture components in rolled fcc materials.

Table 2 lists the identified orientations expressed by their Miller indices and corresponding Euler angles. Combined with the schematic representation of the basic microtextural components, Goss (G):{110}<001>, Brass (B):{110}<112>, Copper (Cu):{112}<111>, S:{123}<634> and A:{110}<111>, and G/B:{110}<114> were the major preferred orientations in this work. The resultant textures are shown in Figure 15. The calculated ODFs in Figures 15a,c obviously demonstrates a more textured material at higher degree of deformation, as also expected based on the orientation maps. In addition to the magnitude of rolling deformation, any changes in the rolling temperature as well as in chemical composition, and mechanical and thermal history, etc. may reflect on the formation of texture [23]. Assuming the constant working temperature (ambient temperature), chemical composition, and initial texture in this case, the magnitude of deformation and the aging treatment are the only influencing factors on the preferred orientation discussed here.

Table 2. Type and crystallography details of the characterized texture components.

Type	Miller indices	Euler angles			Fibre
		ϕ_1	φ	ϕ_2	
Brass (B)	{110}<112>	55	90	45	α/β
Copper (Cu)	{112}<111>	90	35	45	β
S	{123}<634>	59	37	63	β
Goss	{110}<001>	90	90	45	α
A	{110}<111>	35	90	45	α
G/B	{110}<114>	20	45	0	α

Overall view of the ODF sections ϕ_2 =0° of Figure 15a–d shows that the rolling textures are laid in a family of orientations due to the previously identified <110>//ND alignment. An α-fibre, ideally stretching from G:{110}<001> to Rot-G:{110}<011>, tended to form in all specimens. The fibre is fade and depressed in D20 where B:{110}<112>, G:{110}<001> and an orientation close to A:{110}<111> are existing with similar intensities. As the material is more plastically deformed in D50, the α-fibre lacks the intensity of {110}<111>, but appeared more stretched and continuous as shown in Figure 15c. The main fibre constituents,{110}<001> and {110}<112>, in D50 were maintained almost doubled in strength compared to D20.

Moreover, Cu:{112}<111> and S:{123}<634> appeared as the major deformation textures, in the corresponding ODF sections ϕ_2 =45° and ϕ_2 =63° as shown in Figures 15a and 6c, respectively. However,{123}<634> has shown one of the highest strength in all the as-deformed and aged conditions. This is the second tube of orientation (β-fibre) extending from Cu:{112}<111> to

B:{110}<112> while meeting S:{123}<634> along the way in the 3D Euler space. Therefore, two families of deformation textures, *α* and β-fibres, were characterized.

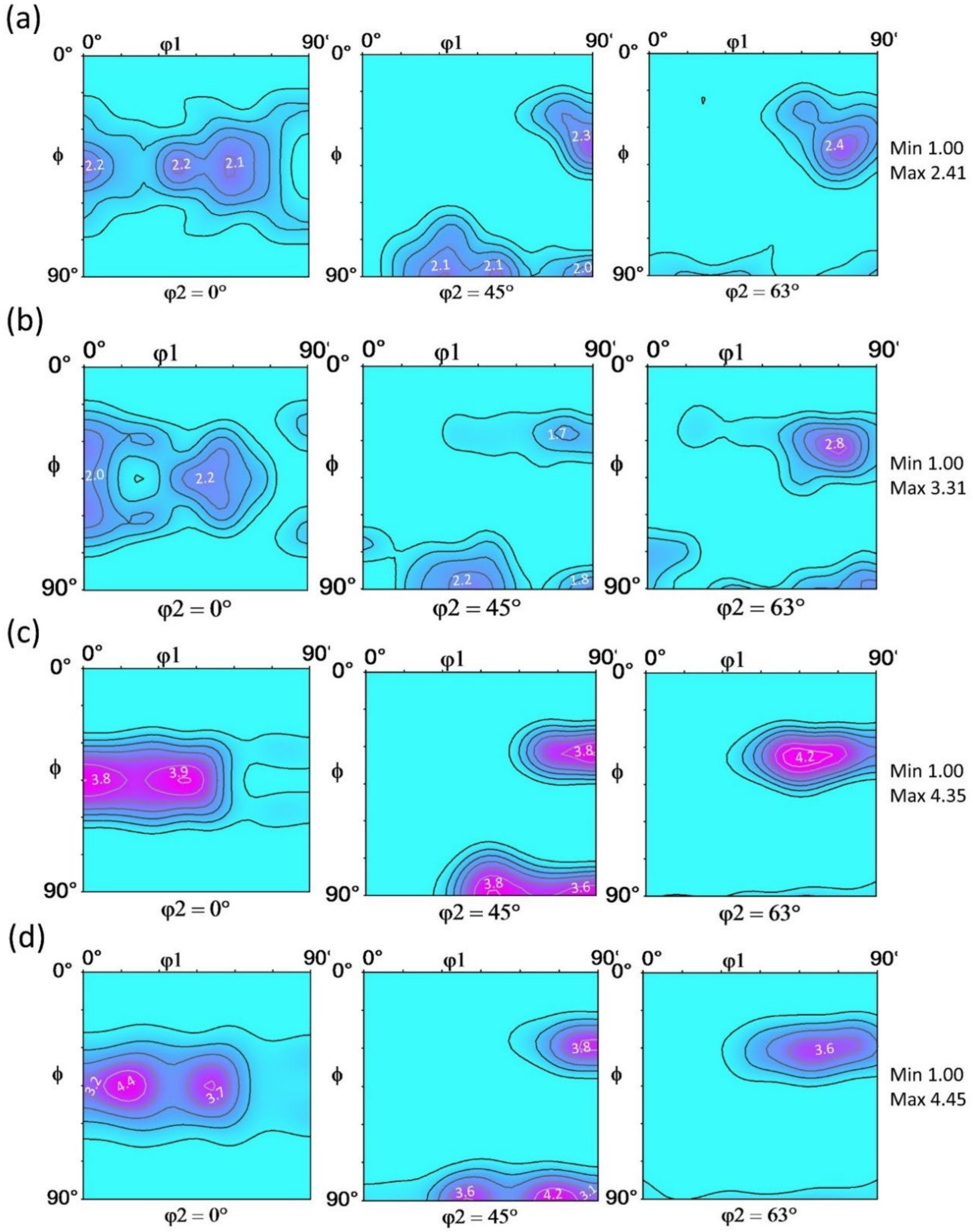

Figure 15. ODF sections of ϕ_2 =0°, 45°, and 63° calculated for; (a)D20, (b)D20A, (c)D50, and (d)D50A.

Figures 15b,d reveals the minor influence of aging on the crystallographic identity of the material, particularly in a less-deformed condition (D20A) compared with the non-aged condition (Figures 15a,c). The fibre nature of the texture is preserved comprising the similar components with slight change in intensities compared to what has already been detected in the as-rolled state. When it comes to highly deformed specimen (D50A), too strong *α*-fibre is split by appearing to decompose the sharp texture continuity. It was adorned by a 4.4 times random of G/B:{110}<114> in ODF section ϕ_2 =0° in Figure 15d. The orientation {110}<112> was depressed and the intensity of {110}<001> fell to

3.2 times random. This can also be observed in the 111 poles' positioning of Figure 13f. In addition, the magnitude of {123}<634> in ϕ_2 =63° dropped to 3.6 times random after the aging heat treatment.

3.6. Fracture Surface Analysis

The SEM images that illustrate typical fractures surfaces of the tensile specimens are shown in Figure 16. D0A (undeformed, aged) exhibits ductile features (a-d) with a few intergranular fractures observed around one of the edges as indicated by white arrows in (c). There are also a few tiny micro voids as shown in (b, c). Large parts of the fracture are however dominated by elongated dimples (d).

Figure 16e–h presents the fracture surface of D20A (20% deformed & aged). The fractures observed are mainly intergranular type that can be micrometers long. Certain parts of the fracture also exhibits clean surfaces without dimples. A magnified view of an area from Figure (f) is shown in (g). Furthermore, the fracture morphology of D20A also includes large and deep microvoids as shown by yellow arrows (h). These features can be cleavage facets corresponding to crystal planes. Both D20A and D50A are dominated by faceted features rather than dimples. The existence of facets and shear suggests localized brittle failure are accountable for the shorter elongation measured in the deformed specimens, especially in D50A.

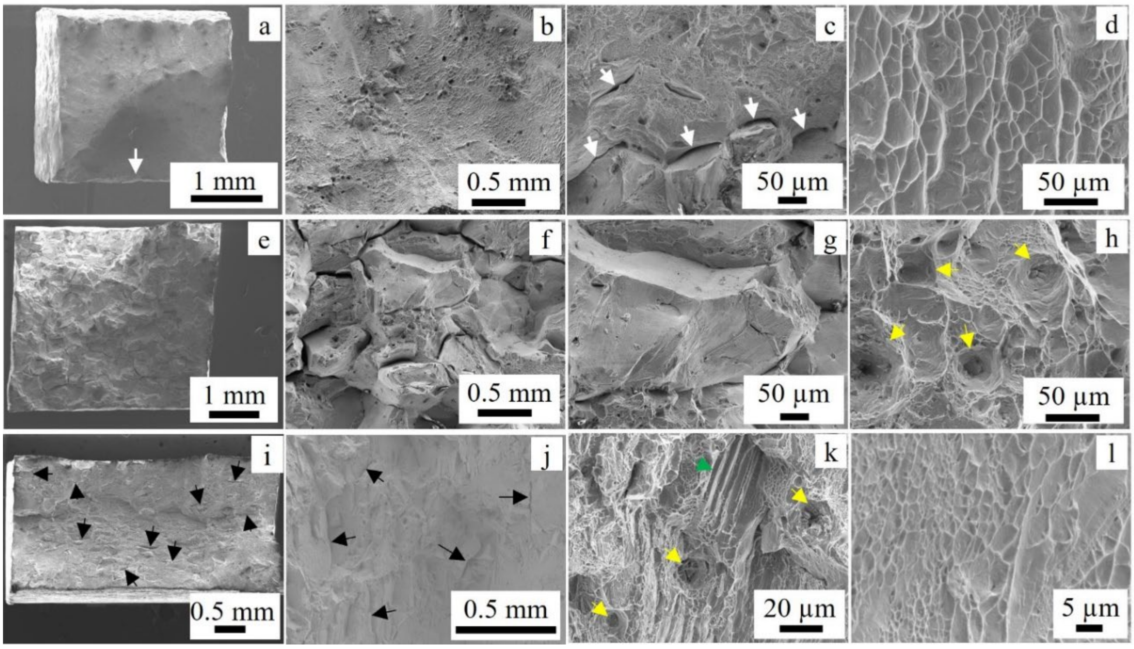

Figure 16. Tensile fracture morphology (a-d) D0A, (e-h) D20A, and (i-l) D50A. The white arrows in (c) are pointing to microcracks near the edge; the black arrows (i, j) are pointing to some of the transgranular cracks in D50A; in (h) are indicating to some of the micropores. Shallow dimples are seen in certain locations of D50 (l). The black arrows are pointing to microcracks, yellow to microvoids, white to an itergranular and green to shear type cracks.

4. Discussions

4.1. Effect of Cold Rolling on Hardening Precipitates

As shown above, cold rolling changes the nucleation, morphology, and distribution of the hardening precipitates compared to the unrolled condition. The nucleation sites of the γ'' and γ' were mainly in the strained region than in the strain-free regions (Figure 7f). The strained regions contain high density of dislocations that trapped atoms. Nb as the main constituent of the γ'' and γ' phases are the heaviest element in the alloy 718, whose motion could be halted by dislocations. The start of nucleation of γ'' precipitates at the dislocation-rich regions in the deformed specimens, in particular in D50A is thus not a surprise. This agrees with the findings of Mei and co-works [11] who found nucleation of γ'' phase near the pre-existing dislocations based on the Differential Scanning

Calorimetry (DSC) measurement. The size of the precipitates in the 50% deformed specimens were however smaller compared to the precipitates formed in the undeformed specimen (8.2±1.6 nm vs. 9.5±2.1) and D20A (8.2±1.6 nm vs. 12.6±3.2). The growth or coarsening can be achieved only if more Nb atoms are coming to the nucleation sites, but the presence of high density of dislocations in the neighbourhood formed barriers to prevent further incoming of Nb atoms. The fact that γ'' precipitates appeared needle/rod-like in morphology implies shortage of Nb atoms for growth to an ellipsoid shape. From the results, it seems that cold rolling to a moderate level (about 20%) facilitates nucleation and coarsening of γ'' than at higher deformation level. As deformation increased to 50%, the size as well as quantity of γ'' precipitates diminished.

4.2. Effects of Cold Rolling on Hardness and Tensile Properties

The cold rolling process significantly changes mechanical strength but reduces ductility of IN718 which can be explained in terms of microstructure and precipitation hardening phases. As shown above, the hardness of the 20% (D20A) and 50% (D50A) rolled/deformed and aged specimens increased by about 42 HV (10%) and 98 HV (23%), respectively, compared to D0A (undeformed, but aged). In order to identify explicitly the factors that affect hardness, the approach of Mei and co-workers [11] is revisited here. The main factors affecting hardness can be distinguished using the empirical formula given in equation (1) [11].

$$HV = HV_S + HV_{WH} + HV_{PH} \quad (1)$$

The subscripts S, WH and PH in the formulation stand for solid solution heat treatment, work hardening and precipitation hardening, respectively. From Figure 9, the hardness value of the specimen after solid solution (D0) is 165 HV. After substituting the measured values in equation (1) for the three cases can be estimated as shown in equation 2-4. Note that the effects of recovery during aging was neglected.

$$HV_{D0A} = 165 + 0 + 275 = 430 \quad (2)$$

$$HV_{D20A} = 165 + 126 + 181 = 472 \quad (3)$$

$$HV_{D50A} = 165 + 252 + 111 = 528 \quad (4)$$

Clearly, hardness increases with increasing percentage of deformation. The hardness of the specimen deformed by 50% enhanced by two folds compared to the specimen deformed by 20%. However, the contribution of precipitation hardening to the hardness is decreasing with increasing percentage of deformation. Relative to the 20% deformed specimen, the hardness of the 50% was decreased by about 63% (70 HV). Similar observation was reported by Mei, et. al. [11]. They have noted an increment in HV_{WH} while reduction in HV_{PH} by increasing the level of rolling from 0% to 70%. Overall, D50A attain the highest hardness compared to D20A and D0A. For the moderate deformation (in this case 20%), the contribution of precipitation hardening is larger than due to the work hardening. This may signal lower density of dislocations occurred compared to the 50% deformed specimen. That is why (work hardening) was the main contributor to the highest hardness obtained in D50A.

The empirical formula applied for hardness can be used to show the effects of rolling on tensile properties, too. Since tensile tests were not done for ST specimens (D0), the first term on the right side of equation (1) can be deleted and write for the UTS by substituting the numerical values given in Figure 10.

$$UTS_{D0A} = 1132 + 0 \quad (5)$$

$$UTS_{D20A} = 1132 + 216 \quad (6)$$

$$UTS_{D50A} = 1132 + 513 \quad (7)$$

The equations (5-7) demonstrate that tensile strength increases with increasing level of deformation. After deformation by 20% (D20A), the UTS increased by 216 MPa (19%) while the UTS of the 50% deformed specimen (D50A) was increased by 513 MPa (45%), compared to that of the undeformed specimen (D0A). Similar trend has demonstrated in yield strength as well. Deformation enhanced yield strength by 242 MPa (25%) for 20% reduction and by 552 MPa (58%) for 50% reduction. The increment in yield strength is more pronounced than UTS, relatively for both deformations. Nanotwins might contribute to the enhanced elastic property of the specimens. Likewise, qualitatively, the concentration level of nanotwins in D50A is higher than in D20A.

The tensile properties obtained from the current work is in most cases better than what have been reported in the literature under the conditions that evolved δ phase (heat treatments, rolling). The maximum UTS, 0.2% YS and elongation measured in this work under 50% deformed condition are 1645 MPa, 1512 MPa, and 3.8 %, respectively. Similarly, the UTS, 0.2% YS and elongation for the 20% deformed specimen are 1348 MPa, 1202 MPa, and 11 %, respectively.

The proportionality of the tensile properties with deformation can be associated with the degree of changes in microstructure. The mechanism of deformation during cold rolling can be understood using TEM analysis. Figure 17 shows the TEM images of the specimens prepared from the RD-ND surface. The BF (a), DF (c, d) and the indexed diffraction pattern (b) reveal presence of high density of twin lamellas that ranges from a few nano meters to several micrometres. As shown in the images, the twins are stacked together in localized bands with the twin planes perpendicular to ND-RD while parallel with <110> orientation. Such nano/microtwins are known for being strong and impenetrable barriers for the dislocation slips as indicated in literature [24]. Since the small spacing between the twin lamellae clearly reduces the mean free path for dislocation slip, the twins enhanced strongly the high strain-hardening rates during cold rolling [25] in addition to dislocations and other lattice defects.

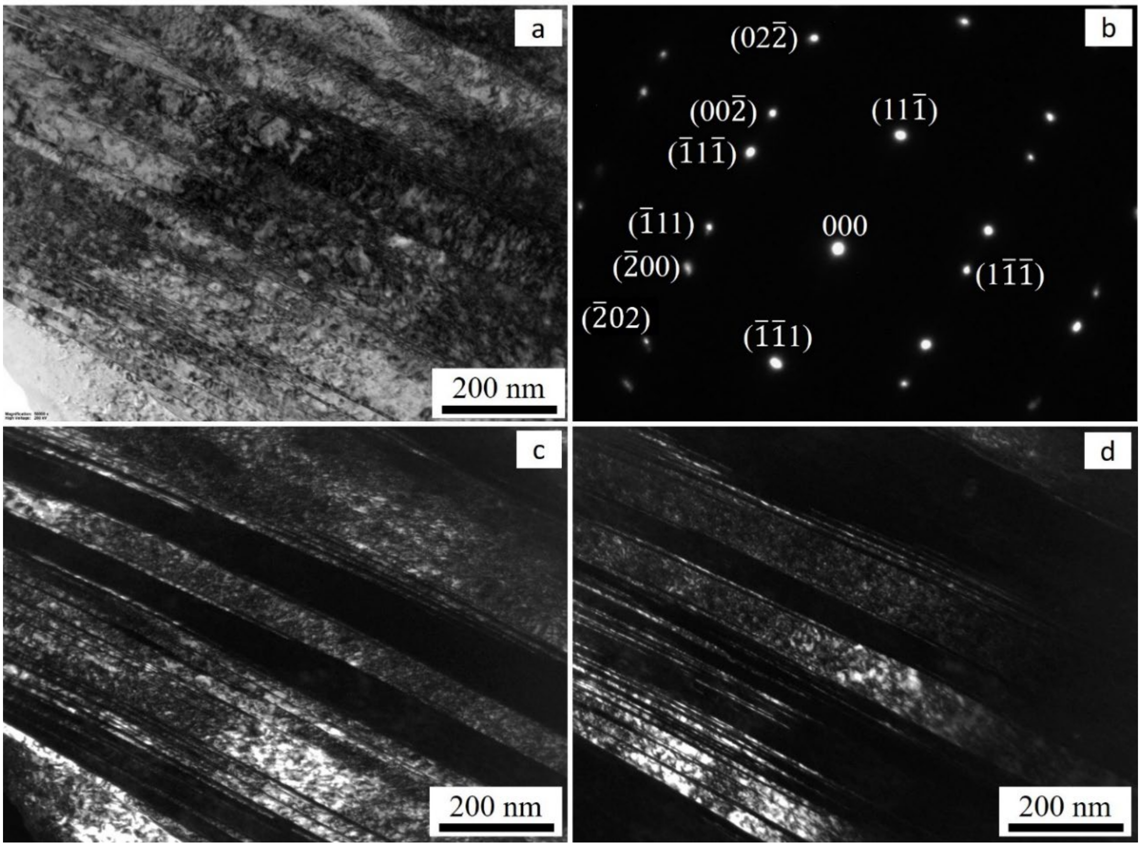

Figure 17. TEM images of cold rolled and aged by 50% (D250A) on the RD-TD surface. (a) Bright field (BF) image, (b) SADP in <110> zone axis (c) dark field (DF) image of the first set of twins (00-2), and (d) DF image of second set of twins using (-11-1) reflection.

4.3. Effects of Cold Rolling on Texture

Crystallographic textures are known to influence most of the mechanical, physical, and chemical properties of alloys. Depending on the value of stacking fault energy (γ_{SFE}) of the FCC materials, two common categories of rolling textures, entitled alloy-type and pure-metal-type, can be emerged. The former is known for low γ_{SFE} materials and promotes strong B along with weakened G, while the latter is typically appeared in medium-to-high γ_{SFE} and includes the identical intensities of Cu, S, and B orientations [26]. Thus, the formation of Cu, S, and B developed on β-fibre and their enhanced intensities under the higher deformation in this work can be correlated to Ni which is known for its high γ_{SFE}. The cross-slip of screw dislocation is behind the development of dominant pure-metal texture. Nonetheless, any decay in the value of γ_{SFE} as a function of solute elements can produce alloy-type texture predominantly induced by mechanical twining, that may subsequently reflect on the intensity of B, and production of G. Assuming the binary system contribution of each element and Ni, and the least influence of Fe, the decrement of γ_{SFE} can be roughly estimated based on the composition of Inconel 718 alloy:

$\Delta\gamma_{SFE}\,\%= 1.66(\text{at. }\%\text{Cr}) + 1.72(\text{at. }\%\text{Al}) + 8.0(\text{at. }\%\text{Ti}) + 1.66(\text{at. }\%\text{Mo}) + 50\%(\text{for} > 0.65 \text{ at. }\%\text{W}) + 0.26(\text{at. }\%\text{Co})$ [27] (8)

Due to the high concentration of Cr, and the simultaneous presence of Mo, Co, Ti, and Al, a considerable reduction of γ_{SFE} is not unexpected. The γ_{SFE} of the alloy falls to the medium level of 67.5 mJm^{-2} after an estimated $\Delta\gamma_{SFE}$ of 42.27%. This could make the solid solution strengthened Inconel 718 alloy highly susceptible to the deformation under the twining mechanism and production of alloy-type texture. As a result, an α-fibre predominantly stretched between {110}<001> and {110}<112> was formed.

5. Conclusions

This work investigates the effects of cold rolling process on the tensile properties and hardness of Inconel 718. Deformation due to cold rolling generally increased hardness and tensile strength significantly but reduces ductility. The results can be summarized as follows:

- The dimension of γ'' precipitate, the main PH phase increased for the 20% deformed, but decreased after 50% deformation and appeared pin/rod like in morphology.
- Cold rolling process increased hardness of the 20% (D20A) by about 42 HV (10%) and the 50% (D50A) deformed specimens by 98 HV (23%).
- The increment in UTS after deformation by 20% (D20A) is 216 MPa (19%), and the increment in UTS for the 50% deformed specimen (D50A) was by 513 MPa (45%).
- Material strength increases with increasing percentage of deformation where contribution by PH decreases while that of WH increases. These can be attributed to the further strained microstructure due to the formation of dislocations and micro twining.
- By 50% deformation, significantly high tensile strength (UTS, YS) can be achieved, but elongation at failure is so low that need modification. A balanced tensile property can be achieved at moderate deformation level (20%).
- Both pure metal-type and alloy-type textures started to form under the cold rolling and their magnitudes was further enhanced at higher deformation. The former generated the β-fibre, consisting {110}<112>, {112}<111>, and{123}<634> which are induced by the cross slip mechanism of dislocations. The latter was shown to be developed by the reduction in stacking fault energy and led to the twining-induced orientation emerged by a predominant <110>∥ND, so-called α-fibre.
- Except minor variations in intensities, no significant changes in the crystallographic nature of the material were observed after the aging operation.

Supplementary information: No supplementary information provided.

Author Contributions: Conceptualization, VH; Investigation, ATS, WMT, NS; writing-original draft preparation, WMT, NS; writing—review and editing, WMT, NS, ATS, and VH; supervision, VH and WM. All authors have read the final version of the manuscript and agreed for submission for publication.

Ethical approval: This work did not involve any animal or human-based research.

Data Availability: The data used for quantification of some of the results can be shared from the corresponding author if requested.

Acknowledgements: The authors would like to thank Scandinavian Fittings and Flanges (SFF) for supplying the specimens used for the study. The second author is grateful to Johan Andreas Håland Thorkaas and Espen Undheim for their assistance in the labs during his M.Sc. project.

Conflict of interest: The authors declare that they have no conflict of interest.

References

1. R Ran, Wang Y, Zhang Y-x, Fang F, Wang H-s, Yuan G, Wang G-d (2020), Microstructure, precipitates and mechanical properties of Inconel 718 alloy produced by two-stage cold rolling method. Materials Science and Engineering: A 793: 139860. Doi:https://doi.org/10.1016/j.msea.2020.139860
2. R Ran, Wang Y, Zhang Y-x, Fang F, Xia Y-k, Zhang W-n, Yuan G, Wang G-d (2022), Two-stage annealing treatment to uniformly refine the microstructure, tailor δ precipitates and improve tensile properties of Inconel 718 alloy. Journal of Alloys and Compounds 927: 166820. Doi:https://doi.org/10.1016/j.jallcom.2022.166820
3. MJ Donachie, Donachie SJ (2002) Superalloys: a technical guide. ASM international,
4. H Qi, Azer M, Ritter A (2009), Studies of standard heat treatment effects on microstructure and mechanical properties of laser net shape manufactured INCONEL 718. Metallurgical and Materials Transactions A 40: 2410-2422. Doi:10.1007/s11661-009-9949-3
5. R Cozar, Pineau A (1973), Morphology of y′ and y″ precipitates and thermal stability of inconel 718 type alloys. Metallurgical Transactions 4: 47-59. Doi:10.1007/BF02649604
6. M Sundararaman, Mukhopadhyay P, Banerjee S (1992), Some aspects of the precipitation of metastable intermetallic phases in INCONEL 718. Metallurgical Transactions A 23: 2015-2028. Doi:10.1007/BF02647549
7. D Paulonis, Oblak J, Duvall D (1969) Precipitation in Nickel-base alloy 718. Defense Technical Information Center,
8. WM Tucho, Hansen V (2018), Characterization of SLM-fabricated Inconel 718 after solid solution and precipitation hardening heat treatments. Journal of Materials Science 54: 823-839.
9. Y Gao, Zhang D, Cao M, Chen R, Feng Z, Poprawe R, Schleifenbaum JH, Ziegler S (2019), Effect of δ phase on high temperature mechanical performances of Inconel 718 fabricated with SLM process. Materials Science and Engineering: A 767: 138327. Doi:https://doi.org/10.1016/j.msea.2019.138327
10. J-l Zhang, Guo Q-y, Liu Y-c, Li C, Yu L-m, Li H-j (2016), Effect of cold rolling and first precipitates on the coarsening behavior of γ″-phases in Inconel 718 alloy. International Journal of Minerals, Metallurgy, and Materials 23: 1087-1096. Doi:10.1007/s12613-016-1326-9
11. Y Mei, Liu Y, Liu C, Li C, Yu L, Guo Q, Li H (2015), Effects of cold rolling on the precipitation kinetics and the morphology evolution of intermediate phases in Inconel 718 alloy. Journal of Alloys and Compounds 649: 949-960. Doi:https://doi.org/10.1016/j.jallcom.2015.07.149
12. S-n Chen, Yang X, Wang B, Li Z, Gao X, Wang B, Tian Y (2023), Effect of deformation and annealing process on microstructure and properties of Inconel 718 foil. Materials Characterization 205: 113322. Doi:https://doi.org/10.1016/j.matchar.2023.113322
13. M Anderson, Thielin AL, Bridier F, Bocher P, Savoie J (2017), δ Phase precipitation in Inconel 718 and associated mechanical properties. Materials Science and Engineering: A 679: 48-55. Doi:https://doi.org/10.1016/j.msea.2016.09.114
14. Y Desvallees, Bouzidi M, Bois F, Beaude N (1994), Delta phase in Inconel 718: mechanical properties and forging process requirements. Superalloys: 281-291.
15. AT Sletsjøe (2023) Effects of cold rolling on the mechanical properties and grain structure of Inconel 718 alloy M.Sc. Thesis M.Sc. Thesis, University of Stavanger
16. B Beausir, Fundenberger J (2017), Analysis Tools for Electron and X-ray diffraction, ATEX-software. Université de Lorraine-Metz 2017.
17. Metallic materials Vickers hardness test Part 1: Test method (2018). ISO 6507-1:2018 Geneva, Switzerland
18. Metallic materials - Tensile testing - Part 1: Method of test at room temperature (2019). ISO 6892-1:2019 Geneva, Switzerland
19. WM Tucho, Hansen V (2021), Studies of post-fabrication heat treatment of L-PBF-Inconel 718: effects of hold time on microstructure, annealing twins, and hardness. Metals 11: 266. Doi:https://www.mdpi.com/2075-4701/11/2/266
20. WM Tucho, Hansen V (2019), Characterization of SLM-fabricated Inconel 718 after solid solution and precipitation hardening heat treatments. Journal of Materials Science 54: 823-839. Doi:10.1007/s10853-018-2851-x
21. L Rongbin, Xianchang H, Mei Y, Wenchang L (2002), Effects of cold rolling on precipitates in inconel 718 alloy. Journal of Materials Engineering and Performance 11: 504-508. Doi:10.1361/105994902770343737
22. S Hong, Chen W, Wang T (2001), A diffraction study of the γ ″phase in INCONEL 718 superalloy. Metallurgical and Materials Transactions A 32: 1887-1901.
23. Texture formation in metal alloys with cubic crystal structures (2016)Taylor & Francis,

24. JM Robinson, Shaw MP (1994), Microstructural and mechanical influences on dynamic strain aging phenomena. International Materials Reviews 39: 113-122. Doi:10.1179/imr.1994.39.3.113
25. L Bracke, Verbeken K, Kestens L, Penning J (2009), Microstructure and texture evolution during cold rolling and annealing of a high Mn TWIP steel. Acta Materialia 57: 1512-1524. Doi:https://doi.org/10.1016/j.actamat.2008.11.036
26. S Suwas, Ray RK (2014) in Suwas S, Ray RK (eds)Crystallographic Texture of MaterialsSpringer London, London
27. XS Xie, Chen GL, McHugh PJ, Tien JK (1982), Including stacking fault energy into the resisting stress model for creep of particle strengthened alloys. Scripta Metallurgica 16: 483-488. Doi:https://doi.org/10.1016/0036-9748(82)90254-X